Response of a Terminally Anchored Polymer Chain to Simple Shear Flow

Richard S. Parnas

Polymers Division, National Institute of Standards and Technology, Gaithersburg, Maryland 20899

Yoram Cohen*

Department of Chemical Engineering, University of California, Los Angeles, California 90024

Received June 6, 1990; Revised Manuscript Received April 9, 1991

ABSTRACT: The behavior of a terminally anchored, freely jointed bead-rod chain subjected to uniform solvent shear flow was investigated via Brownian dynamics simulations. The effects of solvent flow were demonstrated through the dependence of the segment density distributions, components of the radius of gyration, and the attachment force on the solvent shear rate. Additionally, it was found that the effective hydrodynamic thickness was a strong function of the shear rate, in contrast to previous results for bead-spring model chains. Stationary statistical results obtained for the chain extension show two regimes in the configuration space of the model chain, a Brownian regime at low shear rates and a hydrodynamic regime at high shear rates.

1. Introduction and Literature Review

The interaction of surface-bound polymers with flowing fluids is important in a number of applications such as chromatographic separations,[1] biocompatibility,[2] enhanced oil recovery,[3] and the manufacture of composite materials.[4] Knowledge of the conformations that adsorbed or terminally anchored chain molecules attain when subjected to solvent flow is essential for predicting the surface and rheological properties of the polymer layers involved in the above applications.

Experimental studies on the effect of solvent flow on polymers at solid surfaces have relied, primarily, on either the ellipsometric method[5] or the hydrodynamic flow method.[6-9] The ellipsometric technique measures the root-mean-square (rms) thickness of the polymer layer. The hydrodynamic technique measures the increased resistance to flow due to a surface-bound polymer layer and thus gives a measure of the polymer layer thickness commonly referred to as the effective hydrodynamic thickness (EHT). A qualitative summary of the EHT and ellipsometric measurements obtained to date with adsorbed polymer layers is given in Figure 1. Briefly, the ellipsometric experiments[5] with polystyrene (MW = 20 × 10^6) in a Θ solvent showed that the rms polymer layer thickness decreased by about 15% as the shear rate was increased to approximately 8000 s^{-1}. However, polystyrene samples of molecular weight approximately 8.6 × 10^6 and less did not reveal any change in the rms thickness with shear rate.[5] The hydrodynamic measurements in smooth-walled tubes[6] showed that the EHT decreased monotonically for polystyrene and polyacrylamide in good solvents. For polystyrene in a Θ solvent the EHT curve went through a maximum.[6] An increase in the EHT for polymer layers adsorbed from good solvents in smooth-walled pores was observed[9] (not shown in Figure 1), but only when the pore diameter was smaller than the polymer radius of gyration. Measurements with polyacrylamide and polystyrene adsorbed from both good[7,8] and Θ[8] solvents showed that the EHT of an adsorbed polymer layer in porous filters underwent an abrupt increase above a critical strain rate.

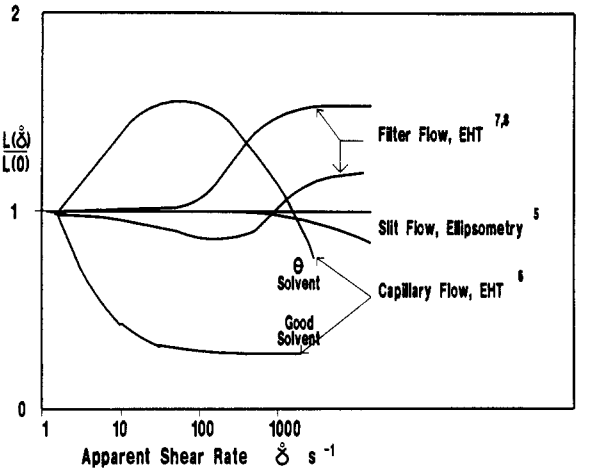

Figure 1. Schematic representation of the trends seen in experimental measurements of polymer layer thickness, L, normalized to the thickness at zero shear rate, $L(0)$: slit flow, ellipsometry[5] (polystyrene: 1 × 10^5 < MW < 20 × 10^6, Θ solvent = cyclohexane at 34.8 °C, surface = polished chrome); capillary flow, EHT[6] (polystyrene: MW = 20 × 10^6, good solvent = toluene, Θ solvent = cyclohexane at 34.8 °C, polyacrylamide: MW = 5.5 × 10^6, good solvent = aqueous NaCl, surface = smooth-walled silica capillaries); filter flow, EHT[7] (polystyrene: 2.4 × 10^6 < MW < 8.2 × 10^6, good solvent = toluene, polyacrylamide: 3 × 10^5 < MW < 8.2 × 10^6, good solvent = aqueous NaCl, surface = Millipore filters); filter flow, EHT[8] (polystyrene: 10 × 10^6 < MW < 48 × 10^6, Θ solvent = cyclohexane at 34.8 °C, polyacrylamide: MW = 7.5 × 10^6, good solvent = aqueous NaCl, surfaces = Nucleopore membranes, sand, and glass beads).

That behavior has been attributed to the possibility that the flow field in the filters contained both shear and elongational components.[5,6,8]

Attempts to explain the interaction between the surface-bound polymer and the solvent flow have progressively evolved from porous-layer models[10,11] to numerical Brownian dynamics simulations.[5,12-15] The porous-layer models describe solvent flow through a surface-bound polymer layer with flow equations that account for the increased resistance to flow due to the presence of the polymer segments.[16,17] The usage of such models requires the segment density profile $\Phi(y)$, or at least the functional

* Author to whom correspondence should be addressed.

0024-9297/91/2224-4646$02.50/0 © 1991 American Chemical Society

form of $\Phi(y)$, in order to estimate the permeability κ as a function of height y above the surface and within the polymer layer. Dejardin and Varoqui[10] assumed an exponential form for Φ (i.e., $\Phi = Ae^{-y/d}$) while Cohen Stuart et al.[11] used the mean field model of Scheutjens and Fleer[18] to compute Φ. It is important to note that in these previous models shear effects on the polymer layer were not considered since the segment density distribution was taken to be invariant with shear rate. The porous-layer models[10,11] predicted that the thickness of an adsorbed polymer layer should vary linearly with the polymer molecular weight, in agreement with the experimental results of Dejardin and Varoqui[10] conducted at shear rates below 200 s^{-1}. Additionally, Cohen Stuart et al.[11] found that the major contribution to the EHT (evaluated from dynamic light scattering) came from the long dangling tails of the polymer that extend far into the solution.

In an effort to understand the role of chain conformation in the relationship between the measured EHT and the shear rate, several simple models of the dynamics of surface-bound macromolecules have been proposed.[5,12-15] These studies have focused on isolated, terminally anchored chains (i.e., polymer tails) or anchored loops. Di Marzio and Rubin[12] and later Fuller[13] concluded that, in simple laminar shear flow, the Hookean bead–spring model for an adsorbed tail (or loop) predicts a bound polymer layer thickness that is invariant with wall shear rate. These previous models were analytically solvable by virtue of the linear spring law used to link the bead to the surface. Improved models, based on the finitely extensible nonlinear elastic (FENE) spring law,[19] predict a bound polymer layer thickness that is invariant to shear rate at low shear rates but that decreases at high shear rates.[5,14,15] Those model predictions indicated that the polymer layer was deformed more easily for shorter chains. The latter trend is opposite to the experimental observation with adsorbed polystyrene in a Θ solvent in which the rms thickness of the adsorbed polymer layer decreased to a greater degree for the higher molecular weight polymers.[5] In an attempt to explain the shear thickening of the adsorbed polymer layer observed by Gramain and Myard,[7] Armstrong and Jhon[20] argued that under some conditions hydrodynamic interactions could destabilize a polymer layer, leading to an expansion of the layer away from the wall, and Atkinson et al.[15] proposed that the shear thickening may be due to elongational flow resulting from surface nonuniformities.

Analytical solutions for the configurational distribution of macromolecules in solution have been obtained for a variety of mechanical models of macromolecules in simple flow fields.[21] The question of wall interactions has also been addressed for the simple dumbbell model.[22] Analytical solutions have also been obtained for models of surface-bound polymers subjected to simple laminar shear flow, but only for Hookean bead–spring models[12,13] and linearized forms of models involving nonlinear spring laws.[5,14] With the advent of large-scale computational facilities, numerical simulations of the detailed dynamics of terminally anchored macromolecules have been made possible for a variety of phenomena and for model macromolecules that are not amenable to analytical treatments.[15,23-25] A number of experimental techniques have been developed to probe macromolecular behavior at interfaces,[26] and these can be used in conjunction with numerical simulations to provide an improved description of interfacial macromolecular dynamics.

To date, the Brownian dynamics studies reported in the literature for terminally anchored chains have been restricted to bead–spring chains.[5,12-15] Although the terminally anchored bead–spring model chains have provided valuable insight into the behavior of surface-bound polymers, they have been unable to satisfactorily describe the experimentally observed polymer response to flow. It has been suggested that freely jointed or freely rotating chain models may provide a more realistic description of the behavior of macromolecules than do bead–spring chain models, especially at large chain deformations.[21,27-29] Although spring constants, which are required in bead–spring models, are not required in flexible bead–rod models to emulate the rheological properties of polymer solutions, the constraint of a constant bead separation distance complicates the mathematical analysis of bead–rod models considerably.[30] Due to the added complexity, bead–rod models have not been widely used in modeling macromolecular dynamics of polymer solutions and have not been previously applied to the problem of surface-bound polymer. Numerical simulations of the dynamics of bead–rod model chains are, however, feasible as was demonstrated in the early study of Gottlieb and Bird for a 3-bead freely jointed chain free in solution[27,31] and the more recent studies of Liu[23] and of Cohen and Parnas[25] for longer freely jointed bead–rod chains.

In the present work, the conformation and effective hydrodynamic thickness of terminally anchored, freely jointed bead–rod model chains (Kramers chains[32]) subjected to solvent flow and under quiescent conditions were studied by Brownian dynamics simulations. More complex macromolecular models that include bond rotational potentials, bond angle restrictions, and other molecular details have been formulated[33-35] for chains free in solution and could be adapted to surface-bound chains. These models have the potential to produce more accurate results than the freely jointed chain model but are more complicated and require significant computational resources. In the current study the freely jointed chain model was adopted as a reasonable compromise between modeling complexity and physical reality. Specifically, we focus on an isolated terminally anchored chain in an attempt to first understand the interaction of a single chain (or noninteracting tails of adsorbed polymer) with solvent flow. Hydrodynamic interactions were neglected, but a porous-layer model was used to estimate the effect of the polymer layer on the solvent flow. It is worth noting that measurements of the effective hydrodynamic thickness of adsorbed polymer layers are most sensitive to the tails of the adsorbed macromolecules.[11] While the tail of an adsorbed polymer chain may change length over time and its interaction with the surface may be very complex due to other competing segments in the adsorbed layer, the terminally anchored chain model explored below provides results of striking similarity to those observed in experiments with adsorbed polymer. Therefore, the current study should also provide an insight into the hydrodynamics of the tails of adsorbed polymer and terminally grafted chains.

2. Model Development

2.1. Model Equations. The freely jointed bead–rod model chain is shown schematically in Figure 2 and a description of this chain model can be found elsewhere.[21] Briefly, the freely jointed chain consists of a sequence of beads linked by fixed-length rods. The rods are connected to the beads via free joints such that the rotation of the rods about the beads is not constrained. However, the chain contour length is constant due to the fixed length of the rods, and this point differentiates bead–rod models

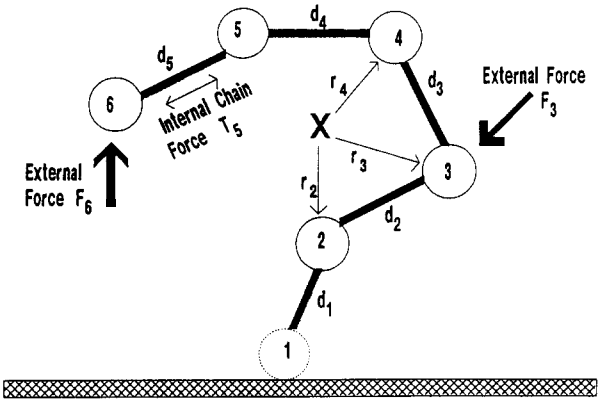

Figure 2. A 6-bead terminally anchored, freely jointed bead–rod chain.

from bead–spring models. The forces **F** acting on the beads in the chain arise from Brownian collisions, hydrodynamic drag, and bead–surface interactions. As a result of the forces applied to the chain, internal chain forces **T** arise in the connecting rods and they are transmitted throughout the chain. The equations governing the motion of the chain are modified Langevin[36] equations which are subject to the constraints of fixed length and rigidity of the rods joining the beads.[23-25,27,28,30-32]

A force balance on each bead in the terminally anchored N-bead chain requires that

$$\mathbf{F}_i + \mathbf{T}_i - \mathbf{T}_{i-1} = m_i\mathbf{a}_i \qquad i = 2, ..., N \tag{1}$$

with $\mathbf{T}_i$ being the internal chain force transmitted along the ith rod. The fixed-length rods require that the separation of adjacent beads along the chain remain fixed at all times, and this constraint may be expressed as

$$|\mathbf{d}_i| = \mathcal{L} \qquad i = 1, 2, ..., N-1 \tag{2}$$

in which $\mathbf{d}_i$ is the position vector between beads i and $i+1$, and $\mathcal{L}$ is the fixed rod length. Furthermore, the internal chain forces are constrained to act along the connecting rods; thus

$$\mathbf{T}_i = T_i\hat{\mathbf{d}}_i \tag{3}$$

and $\hat{\mathbf{d}}_i$ is the unit vector along $\mathbf{d}_i$. The forces **F** applied to the beads may be expressed as

$$\mathbf{F}_i = \mathbf{F}_i^{\,b} + \mathbf{F}_i^{\,h} + \mathbf{F}_i^{\,s} \qquad i = 2, ..., N \tag{4}$$

where $\mathbf{F}_i^{\,b}$, $\mathbf{F}_i^{\,h}$, and $\mathbf{F}_i^{\,s}$ represent forces arising from Brownian motion, viscous drag, and surface interaction effects, respectively[21,37] (see section 2.2).

The model equations, eqs 1–4, may be most conveniently solved by performing a coordinate transformation to internal spherical coordinates. Figure 3a shows the internal spherical coordinate system in which the origin of the spherical coordinates for bead i lies on bead $i-1$. The rotation of bead i about bead $i-1$ is measured by angles θ_i and ϕ_i. The transformation from Cartesian coordinates to the internal spherical coordinates shown in Figure 3a is accomplished by subtracting the force balance, eq 1, for bead i from the force balance equation for bead $i+1$, thereby resulting in the equation for the motion of bead $i+1$ relative to bead i in the r,θ,ϕ coordinate system. The general expressions, in the internal spherical coordinate system, for the θ, ϕ, and r components of the force

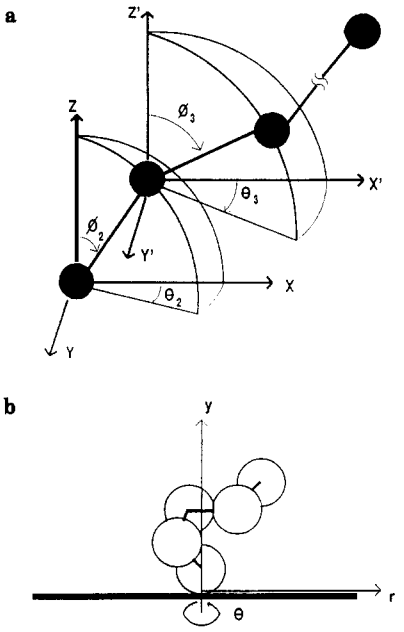

Figure 3. Coordinate systems used to describe the behavior of a terminally anchored chain: (a) internal spherical coordinate system used to compute bead motions; (b) cylindrical coordinate system with origin at the anchoring point used to compute segment densities.

balance on the beads may be expressed as follows:

$$\frac{m|\mathbf{d}_i|\mathrm{d}^2\theta_{i+1}}{\mathrm{d}t^2} = [(\mathbf{F}_{i+1}^{\,b} - \mathbf{F}_i^{\,b}) + (\mathbf{F}_{i+1}^{\,s} - \mathbf{F}_i^{\,s}) + (\mathbf{F}_{i+1}^{\,h} - \mathbf{F}_i^{\,h})]\cdot\hat{\theta}_{i+1} + (-\mathbf{T}_{i-1} + 2\mathbf{T}_i - \mathbf{T}_{i+1})\cdot\hat{\theta}_{i+1} \tag{5}$$

$$\frac{m|\mathbf{d}_i|\mathrm{d}^2\phi_{i+1}}{\mathrm{d}t^2} = [(\mathbf{F}_{i+1}^{\,b} - \mathbf{F}_i^{\,b}) + (\mathbf{F}_{i+1}^{\,s} - \mathbf{F}_i^{\,s}) + (\mathbf{F}_{i+1}^{\,h} - \mathbf{F}_i^{\,h})]\cdot\hat{\phi}_{i+1} + (-\mathbf{T}_{i-1} + 2\mathbf{T}_i - \mathbf{T}_{i+1})\cdot\hat{\phi}_{i+1} \tag{6}$$

$$\frac{m\,\mathrm{d}^2|\mathbf{d}_i|}{\mathrm{d}t^2} = [(\mathbf{F}_{i+1}^{\,b} - \mathbf{F}_i^{\,b}) + (\mathbf{F}_{i+1}^{\,s} - \mathbf{F}_i^{\,s}) + (\mathbf{F}_{i+1}^{\,h} - \mathbf{F}_i^{\,h})]\cdot\hat{\mathbf{d}}_i + (-\mathbf{T}_{i-1} + 2\mathbf{T}_i - \mathbf{T}_{i+1})\cdot\hat{\mathbf{d}}_i \tag{7}$$

where $\hat{\theta}_{i+1}$, $\hat{\phi}_{i+1}$, and $\hat{\mathbf{d}}_i$ are the unit vectors in the internal spherical coordinate system. The solution of eqs 5–7 gives the position and velocity of bead 2 relative to bead 1, bead 3 relative to bead 2, and so forth up to the motion of bead N relative to bead $N-1$. Note that for the case where the subscript $i = 1$, eqs 5–7 simplify because bead 1, which is attached to the surface, is immobile and the terms $\mathbf{F}_1^{\,b}$, $\mathbf{F}_1^{\,s}$, $\mathbf{F}_1^{\,h}$, and $\mathbf{T}_0$ are set equal to zero.

2.2. Simulation of the Applied Forces. In the present analysis, the Brownian forces were simulated with a numerical approximation of white noise.[38] Weiner[39] established that a reasonable form for the stochastic expression of Brownian forces in a large "sea" of solvent is white noise, defined by constant power spectral density and zero autocorrelation.[40] Although the presence of a surface may affect the characteristics of the Brownian fluctuations, the white noise approximation was adopted for lack of a better formulation of Brownian motion near a surface. A convenient way to simulate the Brownian forces is via random numbers. In the current model the $n+1$ random number was generated by[41]

$$\Gamma^{(n+1)} = \text{fractional part of } [\pi + \Gamma^{(n)}]^5 \tag{8}$$

The random numbers Γ, computed from eq 8, must be scaled to properly reflect the level of thermal activity.

The expression of the Brownian forces is then

$$\mathbf{F}^b = (2fkT)^{1/2}\Omega \tag{9a}$$

and

$$\Omega = 2(3^{1/2})(\Gamma - 0.5) \tag{9b}$$

where the mean-squre Brownian force $\langle(\mathbf{F}^b)^2\rangle$ is given by $2fkT$ as shown by Kramers,[37] f is the friction coefficient, k is Boltzmann's constant, and T is absolute temperature. The value 0.5 is subtracted from Γ to produce random numbers that will be positive or negative with equal probability and the factor $2(3^{1/2})$ ensures that $\langle\Omega^2\rangle$ is unity.

Viscous forces on the beads in a model chain arise from their movement through the surrounding solvent. The commonly used method of estimating viscous drag is to adopt a continuum approach[21] and employ a friction coefficient. In the absence of hydrodynamic interactions, the viscous drag on a bead i in the chain is

$$\mathbf{F}_i^h = -f(\mathbf{v}_i - \mathbf{v}_{if}) \tag{10}$$

where $\mathbf{v}_{if}$ is the mass-average fluid velocity at the location of bead i. The friction factor f is assumed to be a scalar quantity and is computed as a Stokes drag coefficient given by[21]

$$f = 6\pi\mu r \tag{11}$$

where μ is the solvent viscosity and r is the bead radius.

In addition to being constrained to an anchoring point on a solid surface, the interactions of the terminally anchored chain with the solid surface must be simulated. The overall effect of simulating the bead–surface interactions is that the model chain is required to occupy only the space above the surface. In the current model, the surface interaction force on bead i is taken to be due to a hard-core repulsive potential between bead i and the surface

$$\mathbf{F}_i^s = \begin{Bmatrix} 0 & \text{if } y_i > r \\ M & \text{if } y_i \le r \end{Bmatrix} \hat{\mathbf{y}} \tag{12}$$

where y_i is the vertical distance of bead i above the surface and $\hat{\mathbf{y}}$ is the unit vector in the vertical direction. Consistent with eq 12, the surface interaction force is set equal to zero if the bead center is located at a distance greater than r above the surface. When the bead center approaches the surface to a distance equal to or less than r, the magnitude of the surface interaction force is set equal to a large constant M (i.e., $|\mathbf{F}_i^s| = M$, where $M \gg 1$). The value of M should be infinity to be entirely consistent with the hard-core repulsive potential. An infinite value of M is impossible to realize in a numerical simulation, and thus a large finite value of M was chosen for computational purposes. The constant M was determined by performing simulations, at increasingly large values of M, until a value of M was found above which the statistical solution was invariant to M.

2.3. Dynamics of a Bead–Rod Chain. The detailed motion of the beads of the terminally anchored model chain is determined by solving eqs 5–7, subject to the simulated forces, eqs 9–12, for the angles θ_i and ϕ_i, as well as the internal chain forces $\mathbf{T}_i$. The values of θ_i and ϕ_i are computed as functions of time by numerically integrating eqs 5 and 6. The internal chain forces $\mathbf{T}_i$ must be found to completely specify the forces applied to each bead in the chain, and they are obtained by considering the r component of the force balance, eq 7, rewritten below with the hydrodynamic drag term $\mathbf{F}^h$ expressed by using eq 10.

$$\frac{m\,d^2|\mathbf{d}_i|}{dt^2} = [(\mathbf{F}_{i+1}^b - \mathbf{F}_i^b) + (\mathbf{F}_{i+1}^s - \mathbf{F}_i^s) + f(\mathbf{v}_{i+1f} - \mathbf{v}_{if})]\cdot\hat{\mathbf{d}}_i - f\,d|\mathbf{d}_i|/dt + (-\mathbf{T}_{i-1} + 2\mathbf{T}_i - \mathbf{T}_{i+1})\cdot\hat{\mathbf{d}}_i \tag{13}$$

The derivative $d|\mathbf{d}_i|/dt$ is the radial component of the bead velocity and the second derivative $d^2|\mathbf{d}_i|/dt^2$ is the radial component of the bead acceleration in the internal spherical coordinate system. The constraint of constant separation distance between the beads, eq 2, requires that the time derivatives in eq 13 be identically zero; thus

$$(\mathbf{T}_{i-1} - 2\mathbf{T}_i + \mathbf{T}_{i+1})\cdot\hat{\mathbf{d}}_i = [(\mathbf{F}_{i+1}^b - \mathbf{F}_i^b) + (\mathbf{F}_{i+1}^s - \mathbf{F}_i^s) + f(\mathbf{v}_{i+1f} - \mathbf{v}_{if})]\cdot\hat{\mathbf{d}}_i \tag{14}$$

The internal chain forces $\mathbf{T}$ may now be expressed as a set of algebraic equations by combining eq 14 with the force transmission constraint given by eq 3

$$\begin{bmatrix} -1 & \hat{\mathbf{d}}_1\cdot\hat{\mathbf{d}}_2 & 0 & 0 & \cdots \\ \hat{\mathbf{d}}_2\cdot\hat{\mathbf{d}}_1 & -2 & \hat{\mathbf{d}}_2\cdot\hat{\mathbf{d}}_3 & 0 & \cdots \\ 0 & \hat{\mathbf{d}}_3\cdot\hat{\mathbf{d}}_2 & -2 & \hat{\mathbf{d}}_3\cdot\hat{\mathbf{d}}_4 & \cdots \\ \vdots & \vdots & \vdots & \vdots & \\ \vdots & \vdots & \vdots & -2 & \\ \vdots & \vdots & \vdots & \hat{\mathbf{d}}_{N-1}\cdot\hat{\mathbf{d}}_{N-2} & -2 \end{bmatrix} \begin{bmatrix} T_1 \\ T_2 \\ T_3 \\ \vdots \\ \vdots \\ T_{N-1} \end{bmatrix} = \begin{bmatrix} \mathbf{f}_{2,1}\cdot\hat{\mathbf{d}}_1 \\ \mathbf{f}_{3,2}\cdot\hat{\mathbf{d}}_2 \\ \mathbf{f}_{4,3}\cdot\hat{\mathbf{d}}_3 \\ \vdots \\ \vdots \\ \mathbf{f}_{N,N-1}\cdot\hat{\mathbf{d}}_{N-1} \end{bmatrix} \tag{15}$$

where the notation $\mathbf{f}_{i+1,i}\cdot\hat{\mathbf{d}}_i$ is an abbreviation for the right-hand side of eq 14, and the set of scalars T_i are the magnitudes of the internal chain forces $\mathbf{T}_i$. The solution of the tridiagonal system of equations for the T_i can be accomplished with a standard sparse matrix solution algorithm.[41]

The internal rearrangements of the chain beads are computed by numerically integrating the θ and ϕ components of the force balance, eqs 5 and 6. To facilitate the numerical integration of eqs 5 and 6, the time derivatives are approximated with second order accurate central differences

$$d\theta/dt = {}^1/_2[\theta^{(t+\Delta t)} - \theta^{(t-\Delta t)}]/\Delta t + \mathcal{O}(\Delta t^2) \tag{16}$$

$$d^2\theta/dt^2 = [\theta^{(t+\Delta t)} - 2\theta^{(t)} + \theta^{(t-\Delta t)}]/\Delta t^2 + \mathcal{O}(\Delta t^2) \tag{17}$$

Analogous equations hold for the approximations of $d\phi/dt$ and $d^2\phi/dt^2$. An approximation for the first derivative of bead position is required due to the appearance of the bead velocity in the viscous drag term, eq 10. Substituting the difference approximations for the derivatives into eqs 5 and 6 provides expressions for computing the values of $\theta^{(t+\Delta t)}$ and $\phi^{(t+\Delta t)}$ from information at time t and at time $t - \Delta t$. For example, the expression for computing $\theta^{(t+\Delta t)}$ is

$$\theta_i^{(t+\Delta t)}\left[1 + \frac{f\Delta t}{2m}\right] - 2\theta_i^{(t)} + \theta_i^{(t-\Delta t)}\left[1 - \frac{f\Delta t}{2m}\right] = \frac{\Delta t^2}{m|\mathbf{d}|}[\mathbf{f} - \mathbf{T}_{i+1} + 2\mathbf{T}_i - \mathbf{T}_{i-1}]^{(t)}\cdot\hat{\boldsymbol{\theta}}_i^{(t)} \tag{18}$$

with a similar equation for the ϕ component. In the absence of hydrodynamic interactions, eq 18 provides an explicit expression for computing $\theta^{(t+\Delta t)}$.

3. Representation of Model Results

3.1. Segment Density Distributions. Model results that are of interest for surface-bound polymer layers include the segment density distributions above the surface and the additional hydrodynamic drag created by the polymer layer when subjected to fluid flow over the surface. For the purpose of expressing the segment density profiles, a cylindrical coordinate system is used with its origin at the chain anchoring point (see Figure 3b). The segment density of a terminally anchored chain is computed in the three-dimensional cylindrical space about the anchoring point. The segment density is defined as the probability $P(R/\mathcal{L}, y/\mathcal{L}, \Theta)$ of finding a bead center at a particular location, normalized such that $[\int\int\int P(R/\mathcal{L}, y/\mathcal{L}, \Theta)\, d(R/\mathcal{L})\, d(y/\mathcal{L})\, d\Theta]/J = 1.0$, where $R/\mathcal{L}$ is the radial distance from the anchoring point and $y/\mathcal{L}$ is the vertical distance above the surface, both nondimensionalized with respect to the segment length $\mathcal{L}$, Θ is the angular position, and J is a normalization constant. The vertical, radial, and angular segment densities can be obtained from the three-dimensional distribution by integration. For example, the vertical segment density distribution is given by $P(y/\mathcal{L}) = \int\int P(R/\mathcal{L}, y/\mathcal{L}, \Theta)\, d(R/\mathcal{L})\, d\Theta$. The effects of flow on a polymer layer may be conveniently expressed in terms of changes in the segment density distributions and the rms values of the distributions. For example, the rms thickness of the polymer layer can be obtained from the vertical segment density profile. The vertical segment density profile can also be used in conjunction with a porous-layer model to compute the effective hydrodynamic thickness as described in the discussion section.

3.2. Radius of Gyration. An additional statistical quantity that is useful in interpreting the Brownian dynamics simulation results is the radius of gyration, R_g. Asymmetries in the configurations of the terminally anchored chain can be clearly displayed with a vectorial interpretation of R_g. The instantaneous square of the radius of gyration, $R_g^2(t)$, is computed as the average of the squared distances of the beads from the center of mass of the chain at time t

$$R_g^2(t) = \frac{1}{N}\sum_i \mathbf{r}_i \cdot \mathbf{r}_i \tag{19}$$

where N is the number of beads in the chain and $\mathbf{r}_i$ is the vector from the chain center of mass to bead i at time t. The time average of $R_g^2(t)$ is the mean-square radius of gyration R_g^2 (i.e., $R_g^2 = \langle R_g^2(t) \rangle$). Expanding the vector dot product $\mathbf{r}_i \cdot \mathbf{r}_i$ in eq 19 in the components of the vectors $\mathbf{r}_i$ and time averaging leads to

$$R_g^2 = x_g^2 + y_g^2 + z_g^2 \tag{20}$$

Thus, R_g^2 is the square of the magnitude of the vector

$$\mathbf{R}_g = x_g\hat{\mathbf{x}} + y_g\hat{\mathbf{y}} + z_g\hat{\mathbf{z}} \tag{21}$$

where $x_g^2 = \langle (\sum x_i^2)/N \rangle$, x_i is the x component of the vector $\mathbf{r}_i$, and y_g and z_g are defined in a manner analogous to the definition of x_g. For a symmetrical chain $x_g = y_g = z_g$, while any asymmetries in the statistical chain conformation will be revealed by inequalities in the gyration components x_g, y_g, and z_g.

3.3. Surface Attachment Force. When a surface-bound chain is subjected to fluid flow, hydrodynamic drag on the chain must be balanced by a surface attachment force which is required to hold the chain to the surface. The surface attachment force is equivalent to the tension $\mathbf{T}_1$ in the rod connecting beads one and two. During the numerical simulations the tension in the rod connecting beads one and two, $\mathbf{T}_1$, is computed at each time step (see eq 15), and the time average of the x component of $\mathbf{T}_1$, $\langle T_{1x} \rangle$, denoted simply as T_x below, is the average surface shear force due to the anchored chain. Adsorbed and grafted polymer layers typically consist of surface chains that interact, and thus a description of the complex hydrodynamics of such surface-bound polymers is not possible with the current approach. Nonetheless, in an effort to understand the relationship between chain conformation and wall shear stress, the current model of an isolated terminally anchored bead–rod chain was used to calculate the wall shear stress for a collection of noninteracting terminally anchored chains. The contribution of a collection of noninteracting chains to the total shear stress at the wall is nT_x, where n is the number of terminally anchored chains per unit surface area. Assuming that the contributions of the solvent and the surface-bound polymer chains are linearly additive, the wall shear stress $(\tau_w)_a$ with a surface-bound polymer layer may be expressed as

$$(\tau_w)_a = \mu\dot{\gamma}_w + nT_x \tag{22}$$

where $\mu\dot{\gamma}_w$ is the contribution to the wall shear stress due to the solvent flow.

4. Results and Discussion

A set of model parameters was chosen to simulate a "generic" polymer and to qualitatively demonstrate the hydrodynamic response of a surface-bound polymer layer. The diameter and mass of the beads were chosen to be 100 Å and 1000 Da, respectively, to correspond with the order of magnitude of the size and mass of the chain segments in a persistence length of a typical polymer. The rod length was chosen to be 100 Å, equal to the bead diameter, giving a "pearl necklace" model chain. The solvent viscosity was set equal to 0.01 P, a typical value for water and other low molecular weight solvents. Lastly, shear rates in the range 0–1000 s^{-1} were employed to determine the response of the model chain to flow, and that range is similar to the shear rates used in experimental investigations.

4.1. No-Flow Cases. Segment density distributions were accumulated for 4-, 5-, 6-, and 10-bead terminally anchored, freely jointed chains under no-flow conditions. Illustrations of the vertical, radial, and angular distributions are shown in Figure 4 for the cases of 5- and 10-bead terminally anchored chains. These distributions were obtained after simulating a period of time sufficient for the distributions to closely approach the statistically stationary state. The angular segment density distributions were used to determine the convergence rate of the simulations to the statistically stationary state. Since, in the absence of flow, the model chain should not be oriented in any preferred direction, the angular distribution of segments about the anchoring point must be flat in the long-time limit. Clearly, as shown in Figure 4b, the angular segment density distributions have become quite flat. Note that this angular segment density does not imply any particular behavior for the distribution of internal chain angles. Since the stationary state of the angular distribution function is known for the case of no flow, the evolution of the angular distribution as the simulation proceeds can be analyzed to provide a quantitative measure of the convergence rate of the simulation results to the stationary state. The rms error in the computed angular distribution is plotted as a function of the simulation time in Figure 5 for the case of the 5-bead terminally anchored chain. After simulating 60 ms, the rms error in the angular distribution function is approximately 0.25%. The slope of the least squares fit straight line in Figure 5 illustrates

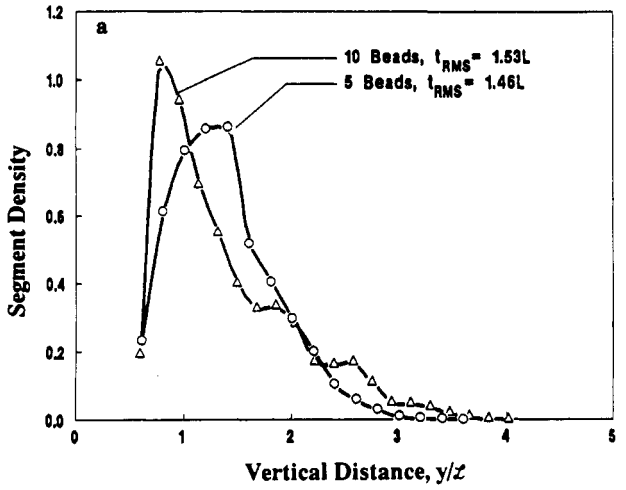

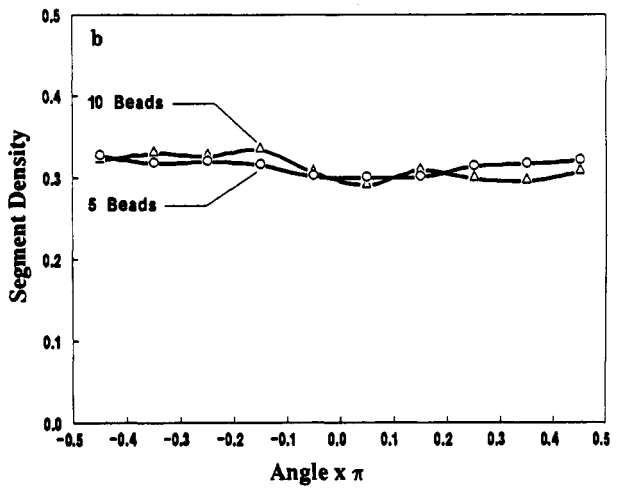

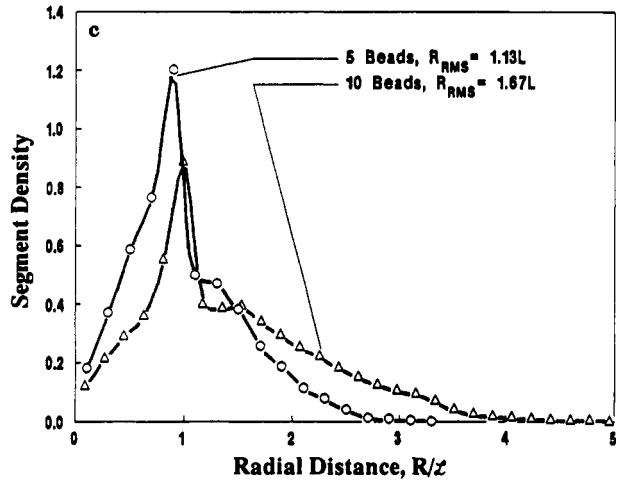

Figure 4. Normalized segment density distributions for a 5-bead and a 10-bead terminally anchored chain under no-flow conditions. The distributions for the 5-bead chain were plotted after simulating 50 ms of time, and the distributions for the 10-bead chain were plotted after simulating 100 ms of time. (a) Vertical segment density. t_{rms} is the root-mean-square vertical extension of the chain. (b) Angular segment density. (c) Radial segment density. R_{rms} is the root-mean-square radial extension of the chain.

that the convergence behavior of the angular distribution follows the theoretical half-power dependence on the simulation time, as expected for random processes.[42] The scatter about the least squares fit line is expected due to the stochastic nature of the simulated process.

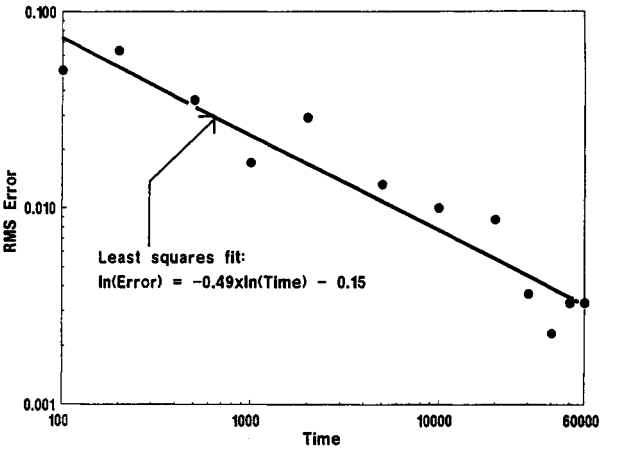

Figure 5. Convergence behavior of the angular segment density distribution function of a 5-bead terminally anchored bead-rod chain. The least-squares fit line indicates a square root convergence rate and the ordinate is RMS error = $\{\sum_1^M [P_c(\theta_i) - P(\theta_i)]^2/M\}^{1/2}$, where P_c is the computed angular density and P is the known statistically stationary angular density.

The vertical and radial distributions (Figure 4a,c) for the 5- and 10-bead chains reveal distinct peaks at approximately 1 segment length from the anchoring point. These peaks are due to the second bead in the chain, which is linked to the anchoring bead. Since the second bead is constrained to a hemispherical surface about the anchoring point, of radius equal to 1 segment length, it contributes strongly to the vertical and radial distributions at distances near 1 segment length from the anchoring point. Prominent shoulders are also visible at about 1.5 segment lengths from the anchoring point primarily due to the third bead in the chain. The vertical segment density distributions are qualitatively similar to the off-lattice Monte Carlo results obtained by Croxton.[43] Croxton[43] attributed the differences in the results obtained with off-lattice and lattice models to the usage of a continuous spatial coordinate system in the off-lattice model.[18,44]

A useful measure of the conformation of terminally anchored chains is the rms thickness and rms radial extension of the chain, as given in Figure 4 for the vertical (Figure 4a) and radial (Figure 4c) segment density distributions. The rms vertical thickness increases by only 4% when the chain length increases from 5 beads to 10 beads. However, Figure 4c shows that the rms radial extension of the chain increases by approximately 50% for the same increase in chain length. Thus, for isolated chains, it is expected that longer chains will extend radially more than vertically, resulting in a flattened conformation. The above conclusion of a flattened conformation for terminally anchored chains at low surface density is consistent with the conclusions from the electron spin resonance study by Hommel et al.[45] for the case of poly(ethylene oxide) grafted onto a silica surface and the infrared measurements of Novotny et al.[46]

It is interesting to compare the rms thickness of the model chain, obtained from the vertical density, to the radius of gyration R_g of an identical chain that is free in solution. For the case of the 5-bead anchored chain, the rms thickness is approximately $1.46\mathcal{L}$, where $\mathcal{L}$ is the segment length. The value of $2R_g$ for a 5-bead model chain free in solution is approximately $1.75\mathcal{L}$;[25,33] therefore, the rms thickness is about 83% of $2R_g$. A similar comparison for a longer 10-bead chain reveals that the rms thickness of a 10-bead terminally anchored chain is approximately $1.53\mathcal{L}$, the value of $2R_g$ of a 10-bead chain free in solution is approximately $2.58\mathcal{L}$,[21] and therefore the rms thickness

of a 10-bead anchored chain is about 59% of $2R_g$ of a 10-bead chain free in solution. These results indicate that the rms thickness of a layer of noninteracting terminally anchored chains, relative to the radius of gyration of chains free in a Θ solvent, decreases with chain length. This trend is opposite to that predicted by Cohen Stuart et al.[11] for the rms thickness of adsorbed layers, relative to the radius of gyration of chains free in solution, under Θ conditions. This difference in predicted trends in the ratio of rms thickness to R_g should not be surprising since the isolated-chain calculations are not expected to accurately approximate the behavior of dense systems under Θ conditions given the importance of entanglement effects in dense layers.[26,29]

4.2. Effects of Flow. The response of a terminally anchored chain to the simple laminar shear flow of a solvent was investigated for terminally anchored bead–rod chains of lengths ranging from 5 to 40 beads at various shear rates. Figure 6 shows the changes that occur in the computed segment density profiles of a 5-bead terminally anchored chain (contour length of 4 segments) as the shear rate over the surface is increased. The vertical density shown in Figure 6a indicates that the chain is squeezed down against the surface as the shear rate increases. The rms thickness decreased from 1.46 segment lengths under no-flow conditions to 1.04 segment lengths at a shear rate of 10 s^{-1} and to 0.82 segment lengths at a shear rate of 100 s^{-1}. The radial density, as depicted in Figure 6b, indicates that the chain is stretched by the shear flow. The radial segment density distribution for the case of a shear flow of 10 s^{-1} shows that the chain is partially extended. The radial density for the case of a shear rate of 100 s^{-1} shows four clear peaks corresponding to the four mobile beads in the chain, indicating that the chain is nearly fully extended. The rms end-to-end distance also indicates that the 5-bead terminally anchored chain subjected to a shear flow of 100 s^{-1} was highly extended since the rms end-to-end distance was approximately 97% of the contour length of the chain. The angular density shown in Figure 6c clearly indicates the chain alignment with the flow at increasingly higher shear rates. As the shear rate is increased, the angular distribution, which was flat in the no-flow case, changes to yield a distinct peak along the flow direction, indicating chain alignment with the flow. Moreover, the peak in the angular density becomes sharper when the shear rate is increased from 10 to 100 s^{-1}, indicating that the chain aligns more closely with the flow at the higher shear rate.

The effects of solvent shear rate on the anchored chain may also be characterized by examining the rms vertical thickness of the model chain. As Figure 7 illustrates, a monotonic decrease of the rms layer thickness with increasing shear rate is evident for the 5-, 10-, 20-, and 40-bead chains. Simulations at zero shear rate for chains longer than 10 beads were not carried out due to the very long times required to reach the statistically stationary state of long chains under no-flow conditions. The curves for the 20- and 40-bead chains indicate, however, that the zero shear rate rms thickness is likely to increase with increasing chain length. At high shear rates where the curves of rms thickness begin to plateau, the rms thickness of the longer chains becomes slightly smaller than the rms thickness of the shorter chains. Longer chains experience more viscous drag due to solvent flow than shorter chains and are therefore dragged down to the surface more strongly. The sigmoidal shape of the curves in Figure 7 indicates that the rms thickness of a polymer layer may have both zero shear rate and high shear rate limits.

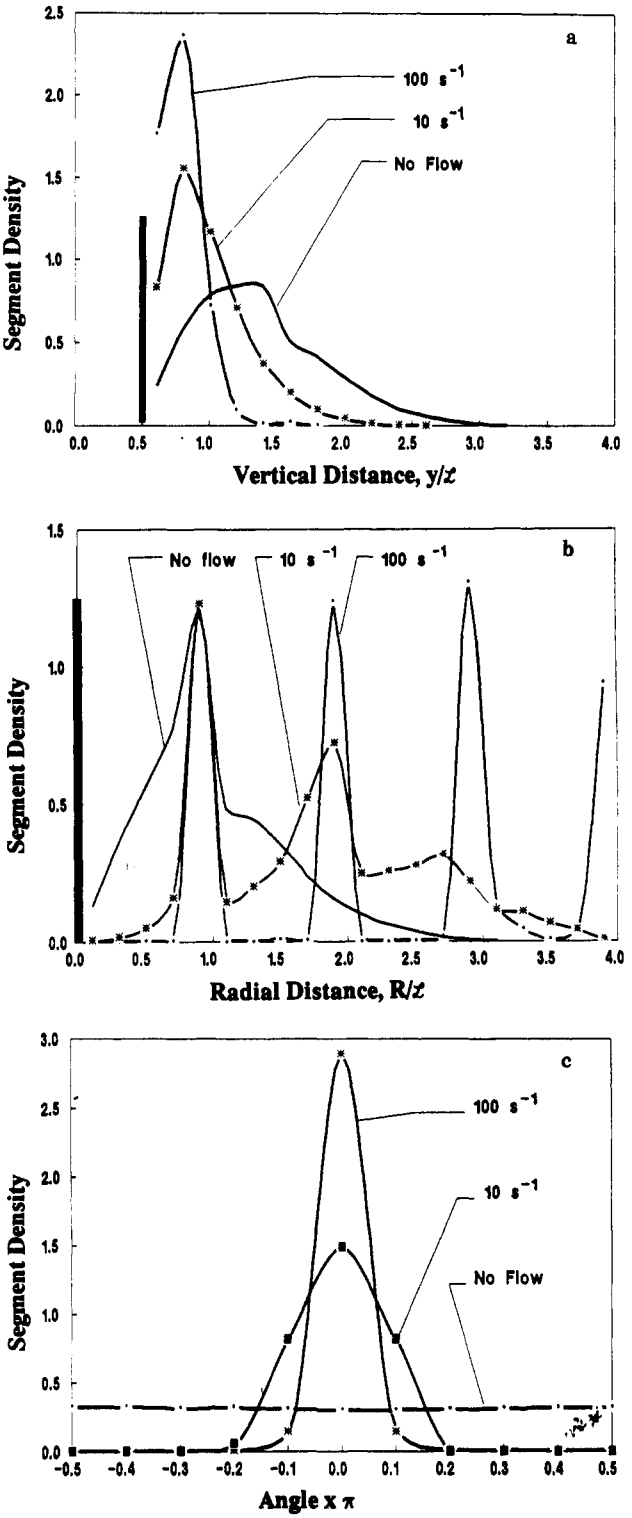

Figure 6. Effects of shear flow on the normalized segment density distributions of a 5-bead terminally anchored chain: (a) vertical segment density at 0-, 10-, and 100-s^{-1} shear rates; (b) radial segment density at 0-, 10-, and 100-s^{-1} shear rates; (c) angular segment density at 0-, 10-, and 100-s^{-1} shear rates.

Moreover, the longer model polymer chains clearly undergo a larger decrease in rms thickness, in accordance with previous ellipsometric measurements.[5] The ellipsometric measurements[5] on adsorbed polystyrene layers revealed the low-shear region of the rms thickness curve where the curve is concave downward. If a high shear rate limit for the rms thickness exists, as indicated in Figure 7, then ellipsometric measurements at higher shear rates than conducted to date may be expected to show a second plateau in rms polymer layer thickness, if flow-induced

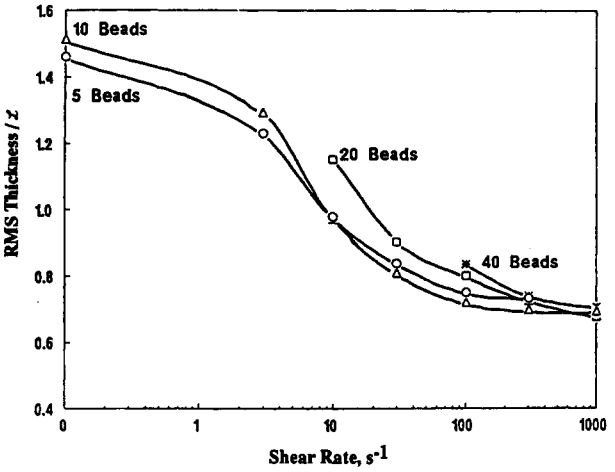

Figure 7. Rms layer thickness as a function of shear rate for 5-, 10-, 20-, and 40-bead anchored chains, nondimensionalized with respect to the segment length $\mathcal{L}$.

desorption does not occur. Due to flow-induced desorption of adsorbed polymer at high shear rates,[47] it may be advantageous to conduct high shear rate experiments with grafted polymer layers.

It is also instructive to quantify shear-induced changes in chain configuration in terms of the time-averaged components of the radius of gyration, x_g, y_g, and z_g, as illustrated in Figure 8 for 5-, 10-, 20-, and 40-bead chains. At shear rates below 3 s^{-1}, the gyration components in the plane of the surface, x_g and z_g, are approximately equal, and the component perpendicular to the surface, y_g, is smaller than the x_g and z_g components. The smaller value of y_g is indicative of the flattened conformation of an isolated terminally anchored chain. As the shear rate increases, the component of the gyration perpendicular to the surface, y_g, decreases as the chain is pushed down against the surface (see also Figure 6a). At the same time the component of the gyration parallel to the flow axis, x_g, increases with shear rate to reflect the chain stretching. Finally, z_g, the component parallel to the surface but perpendicular to the flow axis decreases at shear rates above 3 s^{-1}, reflecting the alignment of the chain with the flow. The z_g component, however, does not vanish at high shear rates because the alignment of the chain by the flow is countered by the randomizing effect of Brownian motion. It is also interesting to note that the inflection points in the x_g and z_g curves suggest a sharp transition in chain extension at shear rates between 30 and 100 s^{-1}. The sharp transition between a coiled and extended configuration (coil–stretch transition) divides the configuration space of the model chains into a weak-flow region dominated by Brownian forces and a strong-flow region dominated by shear forces.

The increase in the asymmetry of the chain configuration with chain length may be quantified at the zero shear rate limit by either of the ratios x_g/y_g or z_g/y_g, since these two ratios should be equal at zero shear rate. The ratio z_g/y_g at the zero shear rate limit, for example, increases from about 1.45 for a 5-bead chain to about 1.73 for a 10-bead chain. Thus, longer isolated chains adopt flatter configurations on the surface in the absence of flow. The increase in asymmetry with chain length is most evident at high shear rates where the ratios x_g/y_g and z_g/y_g must be examined separately due to a three-way asymmetry in chain configuration. The ratio x_g/y_g changes with shear rate for a particular chain length, which reflects the chain stretching in the flow direction as the shear rate is increased. For example, x_g/y_g increases from 1.43 to 9.01 for a 5-bead chain as the shear rate is increased from 0 to 1000 s^{-1}. The ratio x_g/y_g increases from 1.73 to 29.87 in the case of a 10-bead chain as the shear rate is increased from 0 to 1000 s^{-1}, and larger asymmetry ratios, x_g/y_g, occur for the 20- and 40-bead chains. The ratio z_g/y_g does not vary strongly with shear rate for a particular chain length since both z_g and y_g decrease as the shear rate is increased.

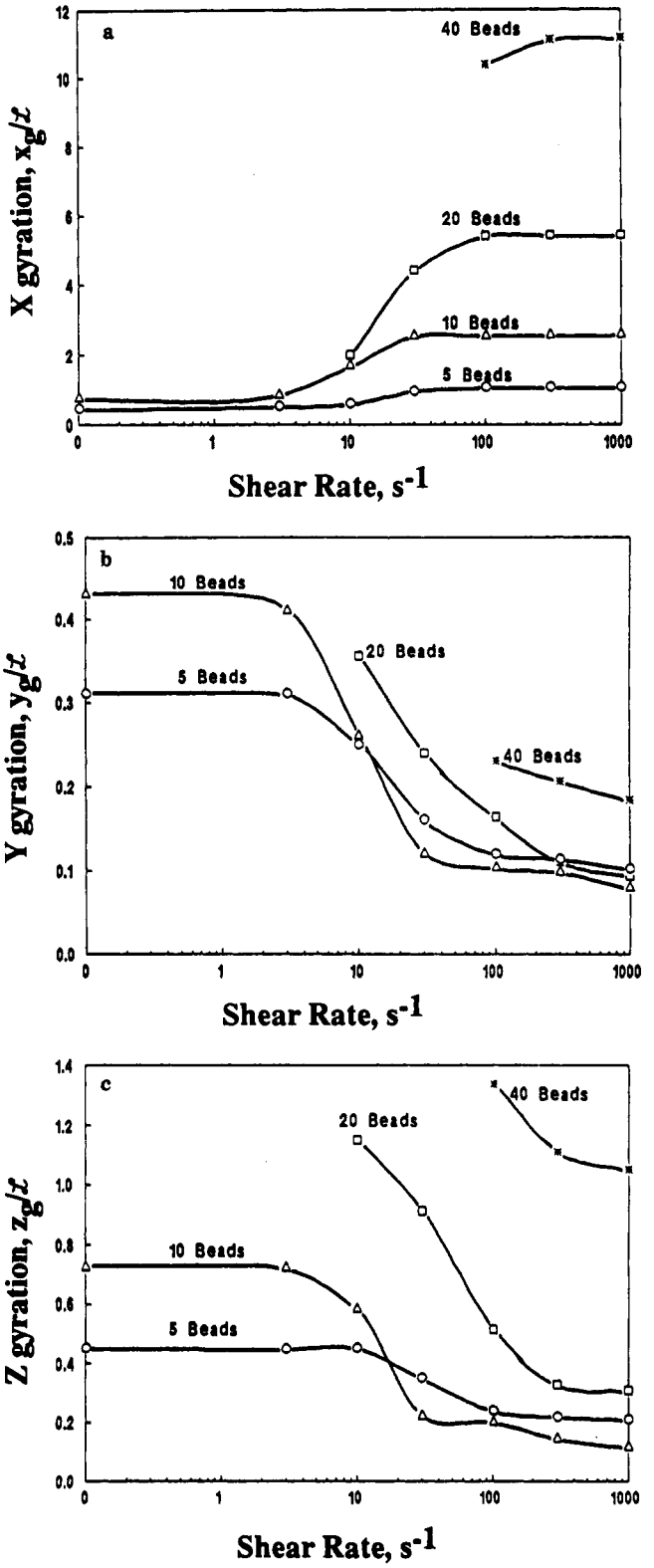

Figure 8. Components of the radius of gyration vector, nondimensionalized with respect to the segment length $\mathcal{L}$, for 5-, 10-, 20-, and 40-bead terminally anchored chains plotted as a function of shear rate: (a) x gyration component; (b) y gyration component; (c) z gyration component.

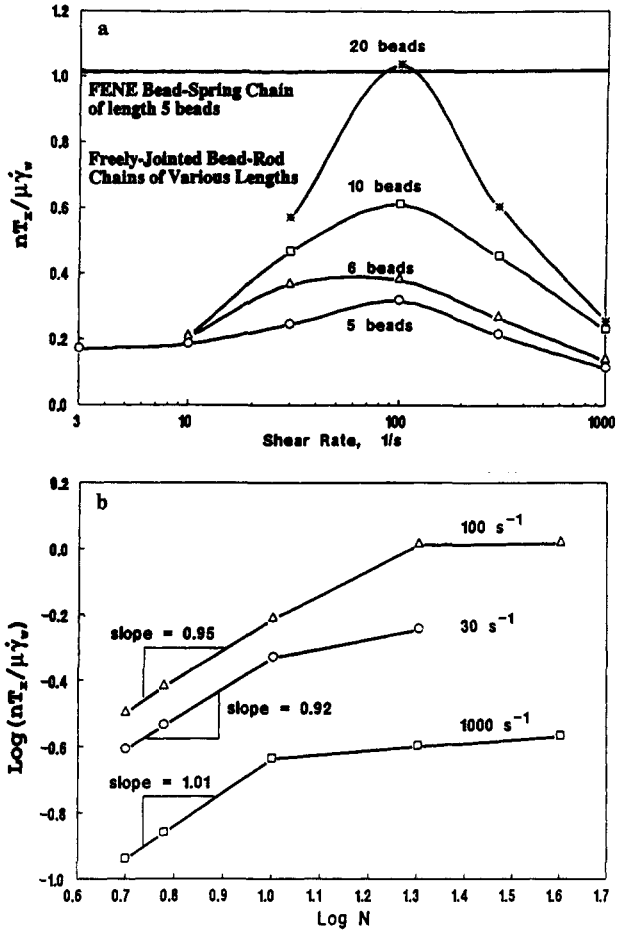

Figure 9. Time-averaged shear force required to hold the terminally anchored chain to its anchoring point scaled by the shear rate: (a) comparison of the time-averaged shear force obtained with the bead–rod model and with the FENE bead–spring model of Atkinson et al.[15] as a function of shear rate; (b) scaling behavior of the time-averaged shear force obtained with the bead–rod model.

The effects of flow on the terminally anchored bead–rod model chain can also be explored in terms of the axial component of the time-averaged attachment force T_x, which is computed by the Brownian dynamics simulations (Figure 9a). It is worth noting that T_x (or the contribution of the terminally anchored chain to the wall shear stress) is a function of the hydrodynamic drag on each bead in the chain and the fraction of that drag which is transmitted through the chain to the surface. The fraction of the axial force that is transmitted through the chain to the anchoring point is affected by the chain conformation. Thus, the wall shear stress generated by flow over a surface-bound polymer layer (eq 22) is also a function of chain conformation, which varies with the imposed shear rate as depicted in Figures 6–8.

The wall shear force values obtained from simulations of the terminally anchored bead–rod chain as well as the wall shear force values recalculated from the results of Atkinson et al.[15] for FENE[19] terminally anchored bead–spring model chains, in the absence of excluded volume and hydrodynamic interactions, are shown in Figure 9a. The attachment force T_x shown in Figure 9a is scaled by the shear rate $\dot{\gamma}_w$ in order to show the relative contribution of the polymer to the wall shear stress. Note that the wall shear stress with a polymer layer, $(\tau_w)_a$, divided by the wall shear stress in the absence of a polymer layer, i.e., $\tau_w = \mu\dot{\gamma}_w$, is given by $(\tau_w)_a/\tau_w = 1 + nT_x/\mu\dot{\gamma}_w$. Since the above results do not consider excluded volume interactions, they are representative of the Θ condition. A quantitative comparison of the results obtained from the different models is not feasible because of the inherent differences in the physical structure of the models.[48] Nonetheless, important features of the trends predicted by the two models are immediately apparent. The terminally anchored bead–spring models[5,14,15] predict a constant value of $nT_x/\mu\dot{\gamma}_w$ at low shear rates and an eventual decline of $nT_x/\mu\dot{\gamma}_w$ at shear rates over 10^4 s^{-1}. In contrast, the terminally anchored bead–rod chain model predicts an increase of the relative wall shear stress $nT_x/\mu\dot{\gamma}_w$ at low shear rates, a maximum in $nT_x/\mu\dot{\gamma}_w$, and then a decline in $nT_x/\mu\dot{\gamma}_w$ with further increases in the shear rate. The maximum in the curve of relative wall shear stress becomes more pronounced for longer chain lengths.

The scaling behavior of $nT_x/\mu\dot{\gamma}_w$ can be explored by plotting the logarithm of $nT_x/\mu\dot{\gamma}_w$ vs the logarithm of the chain length N, as shown in Figure 9b. The quantity $nT_x/\mu\dot{\gamma}_w$ scales with the chain length in a linear manner for chain lengths of up to 10 beads, as indicated by the slopes of the lines given in Figure 9b and in accordance with the results obtained by Dejardin and Varoqui[10] and by Cohen Stuart et al.[11] with adsorbed polymer layers. Figure 9b also indicates that the dependence of the relative wall shear stress on chain length becomes quite weak above a critical chain length which may depend upon the shear rate. Although it would be surprising if the hydrodynamic properties became completely independent of chain length at high molecular weights, a weaker than linear dependence of $nT_x/\mu\dot{\gamma}_w$ on chain length may be explained in terms of the effect of chain conformation on the axial drag T_x. In order for beads (in the anchored chain) that are many segments away from the anchoring point to contribute to T_x, the viscous drag on those beads must be transmitted through the many intervening chain segments to the anchoring point. However, bends and loops in the chain reduce the fraction of stress transmitted through the chain to the anchoring point. Therefore, beads located far from the anchoring point do not contribute strongly to T_x.

The above illustration of the wall shear stress (Figure 9) shows that an important relationship exists between the configuration of a terminally anchored bead–rod chain and the solvent flow. However, the computation of the increase in relative surface shear stress due to the surface-bound polymer layer given above must be regarded as a first-order approximation since the fluid flow field was assumed to be homogeneous shear flow. The presence of the polymer may be expected to retard the fluid flow.

4.3. Effective Hydrodynamic Thickness. As discussed previously, a measure of the increased resistance to flow in a conduit due to the existence of a surface-bound polymer layer is the effective hydrodynamic thickness (EHT). In steady wall-bounded shear flows, the EHT is normally calculated from experimental data based on a comparison of the solvent flows through a conduit (e.g., capillary tube, porous medium) with and without a surface-bound polymer layer.[6,7] The decreased flow due to the presence of the polymer layer is then expressed in terms of the EHT of the surface-bound polymer. Comparing the flows at the same pressure gradient, ∇p, before and after adsorption and making use of the Poiseuille equation for laminar flow in a tube gives

$$L_h/R = 1 - (Q_a/Q)^{1/4} \qquad (23)$$

where L_h is the EHT, R is the tube radius, Q is the solvent flow rate in the absence of the surface-bound polymer, and Q_a is the solvent flow rate in the tube with a surface-bound polymer layer.

The flow in a tube with a surface-bound polymer layer, Q_a, can be predicted with the aid of a porous-layer model in which the permeability of the polymer layer is estimated by utilizing the segment density distributions obtained from the Brownian dynamics simulations. The tube with the wall-bound polymer layer may be considered to consist of two regions, a central region in which flow is unobstructed by the polymer layer and a porous wall region where the flow is partially obstructed by the polymer layer. The solvent flow in the porous wall region can be described by an equation of the form proposed by Debye and Beuche[16,17]

$$\mu\nabla^2 v + \nabla p - (\mu/\kappa)v = 0 \qquad (24)$$

where κ is the permeability of the polymer layer, μ is the solvent viscosity, and ∇p is the pressure gradient. Solution of eq 24 provides the axial velocity $v(y)$ of the solvent flowing through the polymer layer as a function of the position y above the wall. The variation in segment density in a wall-bound polymer layer leads to spatial variation of the permeability κ, necessitating the numerical solution of eq 24. For polymer layers much thinner than the tube radius, curvature effects in the wall region may be neglected. The flow in the central portion of the tube is obtained from the Navier–Stokes equation

$$\nabla p - (\mu/r)\, d(r\, dv/dr)/dr = 0 \qquad (25)$$

and eqs 24 and 25 are solved simultaneously to obtain the coupled flow of solvent in the porous wall region and the central portion of the tube. The solution of eqs 24 and 25 is subject to boundary conditions specifying that the solvent velocity equals zero at the wall and the shear stress equals zero at the center of the tube. Additionally, the solvent velocity and shear stress must be continuous at the interface between the wall region and the central region of the tube in order to couple the solutions obtained by eqs 24 and 25. Additional details of the procedure used to solve the entire flow model are available elsewhere.[3,48]

Values of the permeability in the polymer layer are required to obtain a solution to eq 24, which describes the fluid flow in the porous polymer layer, and these values can be obtained from the segment density distribution generated by the Brownian dynamics simulation. The segment density distribution given by $P(y/\mathcal{L})$ is used to find the volume fraction Φ occupied by beads at height y above the surface

$$\Phi(y) = V_b n N P(y/\mathcal{L})/d \qquad (26)$$

where V_b is the bead volume, n is the number of chains bound to the surface per unit surface area, N is the number of beads in each chain, and d is the diameter of the beads. Following Cohen Stuart et al.,[11] the permeability κ is given by an equation of the form

$$\kappa = c(1 - \Phi)/\Phi \qquad (27)$$

and c is commonly obtained from sedimentation measurements.[49] However, for the theoretical calculations done below, c is taken as $c = \mu/f$, the value appropriate for segments modeled as hard spheres.[10] Once the permeability is obtained from the segment density distribution with eqs 26 and 27 and the velocity profile in the tube is found from the solution of the flow mode given by eqs 24 and 25, the flow in the tube, Q_a, is found by integration

$$Q_a = 2\pi \int_0^R y v(y)\, dy \qquad (28)$$

and the EHT is estimated with eq 23.

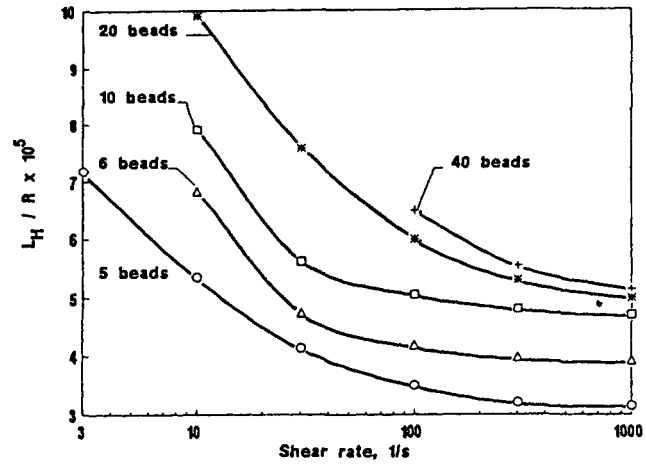

Figure 10. EHT computed from the segment densities obtained from simulations of terminally anchored bead–rod chains of length 5, 6, 10, 20, and 40 beads scaled by the tube radius.

Values of the EHT (L_h), nondimensionalized with respect to the tube radius R, were calculated with eq 23 and are plotted as a function of the shear rate $\dot{\gamma}_w$ for chains ranging in length from 5 to 40 beads in Figure 10. For illustration purposes, the numerical values of L_h/R shown in Figure 10 were obtained for a tube radius of R = 0.01 cm and a surface density of chains of $n = 10^{10}$ chains/cm^2. The assumed value of n was selected to yield values of the bead volume fraction ($\Phi < 0.001$) in accordance with the assumption of noninteracting chains utilized in the Brownian dynamics simulations. The curves of L_h/R vs $\dot{\gamma}_w$ displayed in Figure 10 show a monotonic decreasing trend, just as the curves of rms thickness displayed in Figure 7. However, unlike the curves of rms thickness, the curves of the EHT do not exhibit an inflection point when plotted on a logarithmic shear rate axis. Although the trend in L_h/R resembles the trend seen in the experimental measurements of adsorbed polymer layers in good solvents, it would be premature to claim that the current Brownian dynamics model adequately simulates the behavior of a polymer layer in a good solvent since such polymer layers consist of multiple interacting chains. Nonetheless, the calculations of the EHT for a single isolated chain subjected to an imposed shear flow do convey the importance of the interaction between the surface-bound polymer and the fluid flow.

5. Summary and Conclusions

The freely jointed bead–rod model chain was used to simulate the detailed conformations of isolated, terminally anchored chain molecules subjected to laminar solvent flow. Under no-flow conditions, the results of the current model indicate that isolated, terminally anchored chain molecules have a root-mean-square thickness significantly less than the radius of gyration of an identical chain molecule free in solution, in accordance with the lattice model results of Lal and Stepto[44] and consistent with the experimental results of Hommel et al.[45] and Novotny et al.[46]

The results for the terminally anchored bead–rod chain subjected to solvent flow suggest that macroscopic properties such as the EHT and the polymer contribution to the wall shear stress relative to the stress due to the solvent alone, $nT_x/\mu\dot{\gamma}_w$, are strong functions of the shear rate at low to moderate shear rates. In contrast, bead–spring models predict that the EHT and $nT_x/\mu\dot{\gamma}_w$ are sensitive to the shear rate only at extremely high shear rates. The current model predicts that $nT_x/\mu\dot{\gamma}_w$ increases with

increasing shear rate at low shear rates. Additionally, $nT_x/\mu\dot{\gamma}_w$ goes through a maximum and declines with shear rate at high shear rate levels. The trend predicted in $nT_x/\mu\dot{\gamma}_w$ for a terminally anchored bead–rod chain is explained in terms of a sharp transition in chain extension at a critical shear rate which separates the weak-flow regime dominated by Brownian forces from the strong-flow regime dominated by hydrodynamic forces. The EHT is predicted by the current model to decline steeply as the shear rate is increased, in accordance with the trend observed in the experimental measurements with polymers adsorbed on smooth-walled tubes in good solvents.[6] The reported results can, however, be improved upon by including hydrodynamic interactions to provide more accurate solutions of the fluid velocity profile and segment density distribution within the polymer layer.

The Brownian dynamics model developed in this work is quite general and may be applied in the study of different microscopic environments by modifying eq 4, which is used to compute the forces acting upon the beads in the model chain. For example, the behavior of surface-bound polymer in a good solvent may be simulated by introducing excluded volume interactions.[25] Current studies are underway to incorporate the effects of excluded volume and hydrodynamic interactions.

Acknowledgment. We thank Dr. E. A. Di Marzio for reviewing the manuscript and for his helpful comments and suggestions. This work was funded in part by National Science Foundation Grant CBT-8416719, the National Science Foundation Engineering Research Center on Hazardous Substance Control (Grant CDR-86-22184) and the U.S. Geological Survey, Department of the Interior (Award No. 14-08-0001-G1315).

References and Notes

(1) Yau, W. W.; Kirkland, J. J.; Bly, D. D. *Modern Size Exclusion Chromatography*; John Wiley & Sons: New York, 1979.
(2) Andrade, J. D. In *Surface and Interfacial Aspects of Bio-medical Polymers*; Andrade, J. D., Ed.; Plenum: New York, 1985; Vol. 2.
(3) Parnas, R. S.; Cohen, Y. *Chem. Eng. Commun.* **1987**, *53*, 3.
(4) Lee, M. H. *J. Appl. Polym. Sci.* **1987**, *33*, 2479.
(5) Lee, J. J.; Fuller, G. G. *Macromolecules* **1984**, *17*, 375.
(6) Cohen, Y. *Macromolecules* **1988**, *21* (2), 494.
(7) Gramain, Ph.; Myard, Ph. *Macromolecules* **1981**, *14*, 180.
(8) Bagassi, M.; Chauveteau, G.; Lecourtier, J.; Englert, J.; Tirrell, M. *Macromolecules* **1989**, *22* (1), 262.
(9) Idol, W. K.; Anderson, J. L. *J. Membr. Sci.* **1986**, *28*, 269.
(10) Dejardin, P.; Varoqui, R. *J. Chem. Phys.* **1981**, *75* (8), 4115.
(11) Cohen Stuart, M. A.; Waajen, F. H. W. H.; Cosgrove, T.; Vincent, B.; Crowley, T. L. *Macromolecules* **1984**, *17*, 1825.
(12) Di Marzio, E. A.; Rubin, R. J. *J. Polym. Sci.* **1978**, *16*, 457.
(13) Fuller, G. G. *J. Polym. Sci., Polym. Phys. Ed.* **1983**, *21*, 151.
(14) Hatano, A. *Polymer* **1984**, *25*, 1198.
(15) Atkinson, J. D.; Goh, C. J.; Phan-Thien, N. *J. Chem. Phys.* **1984**, *80* (12), 6305.
(16) Debye, P.; Beuche, A. M. *J. Chem. Phys.* **1948**, *16*, 573.
(17) Anderson, J. L.; Kim, J. O. *J. Chem. Phys.* **1974**, *86* (9), 475.
(18) Scheutjens, J. M. H. M.; Fleer, G. J. *J. Phys. Chem.* **1979**, *83* (12), 1619.
(19) Warner, H. R. *Ind. Eng. Chem. Fundam.* **1972**, *11*, 379.
(20) Armstrong, R.; Jhon, M. S. *J. Chem. Phys.* **1985**, *82*, 2475.
(21) Bird, R. B.; Hassager, O.; Armstrong, R. C.; Curtiss, C. F. *Dynamics of Polymeric Fluids*; Wiley: New York, 1987; Vol 2.
(22) Petruccione, F.; Biller, P. *J. Rheol.* **1988**, *32* (1), 1.
(23) Liu, T. W. *J. Chem. Phys.* **1989**, *90* (10), 5826.
(24) Cohen, Y.; Parnas, R. S. *Polym. Prepr. (Am. Chem. Soc., Div. Polym. Chem.)* **1989**, *30* (1), 385.
(25) Parnas, R. S.; Cohen, Y. *J. Chem. Phys.* **1989**, *90* (11), 6680.
(26) Cosgrove, T.; Vincent, B. In *Fluid Interfacial Phenomena*; Croxton, C. A., Ed.; John Wiley & Sons: New York, 1986.
(27) Gottlieb, M. *Comput. Chem.* **1977**, *1*, 155.
(28) Hassager, O. *J. Chem. Phys.* **1974**, *60*, 2111.
(29) Doi, M.; Edwards, S. F. *Theory of Polymer Dynamics*; Oxford University Press: Oxford, 1986.
(30) Fixman, M. *Proc. Natl. Acad. Sci.* **1974**, *71* (8), 3050.
(31) Gottlieb, M.; Bird, R. B. *J. Chem. Phys.* **1976**, *65*, 2467.
(32) Kramers, H. A. *Physica* **1944**, *11*, 1.
(33) Flory, P. J. *Statistical Mechanics of Chain Molecules*; Interscience Publishers: New York, 1969.
(34) Helfand, E. *Workshop on Dynamics of Macromolecules Symposium, J. Polym. Sci., Polym. Symp. 73* **1985**, *39*, 1.
(35) Kirkwood, J. G.; Riseman, J. *J. Chem. Phys.* **1948**, *16*, 565.
(36) Langevin, P. *C. R. Seances Acad. Sci.* **1908**, *146*, 530.
(37) Kramers, H. A. *Physica* **1940**, *7*, 284.
(38) Einstein, A. *Ann. Phys. (Leipzig)* **1905**, *17*, 549.
(39) Wiener, N. *Acta Math.* **1930**, *55*, 117.
(40) Gardiner, C. W. *Handbook of Stochastic Methods*, 2nd ed.; Springer-Verlag: New York, 1985.
(41) Cheney, W.; Kincaid, D. *Numerical Mathematics and Computing*, 2nd ed.; Brooks/Cole: Monterey, 1973; Chapter 9.
(42) Hammersley, J. M.; Handscomb, D. C. *Monte Carlo Methods*; Chapman and Hall: London, 1979; p 45.
(43) Croxton, C. A. In *Fluid Interfacial Phenomena*; Croxton, C. A., Ed.; John Wiley & Sons: New York, 1986; Chapter 7.
(44) Lal, M.; Stepto, R. F. T. *J. Polym. Sci., Polym. Symp. 61* **1977**, *401*, 1.
(45) Hommel, H.; Legrand, A. P.; Tougne, P.; Balard, H.; Papirer, E. *Macromolecules* **1984**, *17*, 1578.
(46) Novotny, V. J.; Hussla, I.; Turlet, J. M.; Philpott, M. R. *J. Chem. Phys.* **1989**, *90* (10), 5861.
(47) Fuller, G. G. *ACS Symp. Ser.* **1984**, *240*, 67.
(48) Parnas, R. S. Ph.D. Thesis, University of California at Los Angeles, 1990.
(49) Mijnlieff, P. F.; Jaspers, W. J. *Trans. Faraday Soc.* **1971**, *67*, 1837.